Brief Communication

An electronic synaptic memory device based on four-cation mixed halide perovskite

Michalis Loizos[1], Konstantinos Rogdakis[1,2,*], Emmanuel Kymakis[1,2,*]

* Email addresses: krogdakis@hmu.gr, kymakis@hmu.gr
[1]Department of Electrical & Computer Engineering, Hellenic Mediterranean University (HMU), Heraklion 71410, Crete, Greece
[2]Institute of Emerging Technologies (i-EMERGE) of HMU Research Center, Heraklion 71410, Crete, Greece

Abstract

Organic-Inorganic Halide Perovskites (OIHP) have attracted tremendous research interest due to their exceptional semiconducting properties in combination with their facile, solution-based manufacturing performed at low-temperatures. Their device applications cover a wide range of domains, while amongst them, photovoltaics is one of the most promising paths towards industrialization. The complex ionic character of perovskites offers a gigantic playground of new dynamic phenomena such as migration of ionic species and vacancies that are strongly coupled to electronic carriers. The interactions between ions and charge carriers are commonly tunable by electrical fields, light, and strain, opening the path for novel device concepts with emerging functionalities. Here, we study the synaptic properties of a four cation RbCsFAMA perovskite device deployed across an inverted solar cell geometry, as an expansion of *Rogdakis et al. Mater. Adv., 2022, 3, 7002* investigations. The device exhibits stable bipolar resistive switching behavior and operates in a low voltage window < ±1V, with a high resistance to low resistance state ratio of up to 10^5. We show that our device can emulate a wide variety of synaptic functions such as paired-pulse facilitation, long-term potentiation, long-term depression, spiking-rate-dependent plasticity, and spike-timing-dependent plasticity.

1 Introduction

In an evolving world where the demand for information storage and meaningful data processing is increasing, the Internet of Things (IoT) offers a potential solution. In IoT platforms, a network of interconnected devices such as sensors and wearables can receive and exchange information, while should be capable of processing large amounts of data to avoid often communication with the cloud that is time and energy costly [1]. Computation hardware based on traditional von Neumann architecture faces severe limitations to handle these big data demand due to Moore's law and the memory bottleneck [2,3].

The human brain contains roughly 10^{12} Neurons ,which are connected through 10^{15} synapses [4] that transfer information between neurons. Synapses can evolve depending on the activity of the connecting

neurons, showing therefore a dynamic plasticity [5,6]. Synaptic plasticity is considered the foundation of learning and memory [7]. In addition, the human brain can distribute information via multiple pathways, enabling parallel processing [8] that is a unique feature going beyond CMOS-based technologies. Neuromorphic computing therefore relies on the design of devices/computing chips, both at hardware and architecture level, that emulate functions of biological synapses: they use low-power, analog computational elements, massively parallel architectures, asynchronous event-based communication, and "slow" signal transmission rates (e.g., tens of Hz as opposed to hundreds or thousands of MHz) [9]. In a neuromorphic system, the artificial synapse is the fundamental processing unit.

Various devices have shown characteristics resembling an artificial synapse involving resistive switching memories [10–12], transistors [13–15], phase change memories [16,17], and ferroelectric tunnel junctions [18,19]. Memristors or resistive switching memories are typically two-terminal devices in analogy to biological synapses, hence are suitable for brain-inspired computing applications. Resistive switching devices cover a wide range of applications including information storage that has attracted commercial interest[20–22], neuromorphic devices [23,24] and neural network applications [25,26]. Furthermore, memristor crossbar arrays can be used to perform vector-matrix multiplication for neuromorphic computing applications, providing the advantages of in-memory-computation [27].

A wide range of materials are used in synaptic devices, such as 2D materials [28–30], organic materials[31,32], and organic-inorganic halide perovskites (OIHP) [33,34]. Specifically, Wang et al. demonstrated a ZnO-based optoelectronic memristor capable of performing neuromorphic tasks such as face recognition with an accuracy of 86.7% [35]. Zhong et al. fabricated a Ti/(TiO_x/TaO_y)/Pt Memristor with 99.6% accuracy in recognizing spoken digits [36]. Gong et al. achieved an accuracy of 88.2% in recognizing handwritten digits based on a sequentially deposited $FAPbI_3$ perovskite artificial synapse[37]. Wang et al. demonstrated a 2H-MoS_2 nanosheet-based memristor and artificial synapse with 90.37% accuracy of pattern recognition with handwritten data [38]. Finally, Lee et al. developed an organic resistive switching device with an 92.4% accuracy in recognizing handwritten digits [39].

Resistive switching memories can alter their current flow, while the modulation of their resistance depends on the switching mechanism being either an interface- or filament-based. Continuous changes in memristor current flow are equivalent to the synaptic weight changes of an artificial synapse. State-of-the-art resistive random access oxide memories (RRAM) offer a large ratio of high resistance state (HRS) to low resistance state (LRS) reaching values above 10^2, a fast switching speed <10ns with low energy consumption of <0.1 pJ per switching event, and states retention >10 years with good thermal stability[40]. However, the device manufacturing process often involves high-temperature and complex processing techniques[41].

In recent years, OIHPs have attracted tremendous research interest due to their exceptional optoelectronic properties such as high absorption coefficients, tunable bandgap, long diffusion lengths, ambipolar charge transport, and high carrier mobility [42–46]. The formation of perovskite films is based on solution-processable techniques implemented at low temperatures, enabling the fabrication of various flexible device types: photovoltaics [47], light-emitting diodes (LEDs) [48], sensors [49], resistive switching memories [50], photodetectors [51], and field-effect transistors [52], just to name a few. The main focus on these devices is perovskite solar cells, where their impressive and continuous progress has led to efficiencies above 25% [53,54]. Neuromorphic computing is another application domain of perovskite electronics that further spans their use beyond photovoltaics [55]. While hysteresis phenomena are a drawback for many perovskite devices, it appears that they are beneficial for resistive switching memories and synaptic devices. Hysteresis in perovskites has three possible origins: 1) charge trapping or

de-trapping by bulk or surface defects, 2) ferroelectric polarization, and 3) ion migration [56]. Since the more mobile species in OIHP are halides, resistive switching effects originate from iodide or bromide vacancy migration in analogy to oxygen vacancy migration in binary oxide memories [57–60].

A characteristic beneficial property of OIHP synaptic devices is their low power consumption. Ku et al. demonstrated a two-terminal $CH_3NH_3PbI_3$ synaptic device requiring only 47 fJ/μm^2. Xiao and Huang fabricated a memristive device having the structure of ITO/PEDOT: PSS/ $CH_3NH_3PbI_3$/Au that mimics the synaptic learning rules of spike-timing-dependent plasticity (STDP), spike-rate-dependent plasticity (SRDP), and long-term potentiation (LTP). The device required few fJ per $(100nm)^2$ per switching event [61]. Another beneficial property of OIHP is their enhanced optical response, leading to light-stimulated synaptic devices [62]. Ma et al. investigated the synaptic properties of a device based on $CsPbBr_3$ nanoplates (PNs) using the structure of ITO/PEDOT: PSS/CuSCN/$CsPbBr_3$ PNs/Au. The synaptic device had a memory backtracking function that enabled optoelectronic neuromorphic computing applications [63]. Numerous OIHP compounds have been used for artificial synapses including organometal halide [62], layered perovskites with dimensionality-dependent plasticity [64,65], all-inorganic [66], and lead-free $A_3B_2X_9$(B=Bi, Sb) compounds [67]. Although many reports have investigated the synaptic properties of OIHP compounds, a small fraction of these studies has focused on mixed-cation systems. John et al. studied and compared the synaptic properties of MA, FA and Cs-based systems and explained their behavior based on halide vacancies mediated by an ion drift-diffusion process [68]. In our previous work by Rogdakis et al. [61], we have shown that a complete memristive photovoltaic material stack based on a 4-cation OIHP could simultaneously perform solar energy harvesting and neuromorphic functions. Hereby, we extend the investigations on the synaptic properties of this resistive switching memory device by emulating paired-pulse facilitation (PPF), long term potentiation (LTP), long-term depression (LTD), spike-rate-dependent plasticity, and spike-timing-dependent plasticity (STDP).

2 Results and Discussion

Figure 1a shows a typical structure of the artificial synaptic devices consisting of ITO/PTAA/RbCsFAMA/PCBM/BCP/Ag. This structure can efficiently harvest energy as it can operate as a solar cell (exhibiting a power conversion efficiency >17%), while can concurrently emulate neuromorphic functions [61]. Figure 1b illustrates the schematic of a biological synapse and its components, namely dendrites, the body, and an axon. Neurons are connected through synapses, where signal transmission evolves through a pre-synaptic and a post-synaptic neuron and a synaptic cleft between the axon of one neuron and the dendrites of the other. In a chemical synapse, when the pre-neuron receives an electric signal or action potential, ion channels (K^+,Ca^{2+}, Na^+) open and release neurotransmitters towards the post-neuron, converting the electric signal to a chemical, hence leading to its transmission to another neuron [69,70]. In this regard, the Ag top electrode and the ITO bottom electrode resemble the pre-and post-synaptic neurons, where the RbCsFAMA perovskite layer represents the synapse where signal transmission occurs. The continuous resistance changes in these memory devices are equivalent to the synaptic weight change and can be modulated by applying consecutive electrical spikes [71].

An electroforming step of 2V is initially required to set the device from a pristine HRS to a LRS, where a conductive filament is formed between the Ag top electrode and ITO bottom electrode. According to our previous study and literature reports, the filament originates mainly from the migration of iodide vacancies and Ag ions [72–74]. Upon filament formation, the device exhibits stable, bipolar resistive switching behavior. Figure 2a and 2b depict 30 resistive switching loops of the RbCsFAMA device both in

logarithmic and linear scale, respectively. The SET process occurs when the device switches from HRS to the LRS at 0.22±0.06V on average, while the RESET process occurs when the device switches from HRS to LRS at approximately -0.97±0.09V, showing that the device operates below ±1V. The ON/OFF ratio can reach up to 10^5 (HRS/LRS at 200mV in Figure 2a). During all measurements, a compliance current of 10mA is set to prevent the dielectric breakdown of the device. Figure 2c depicts four consecutive current-voltage sweeps from 0V to 700mV to 0V. This figure shows the current tunability of the device towards different resistance states during sequential scans. This behavior corresponds to synaptic weight gradual enhancement and shows that the conductance of the device can be controlled by sequential electrical pulses.

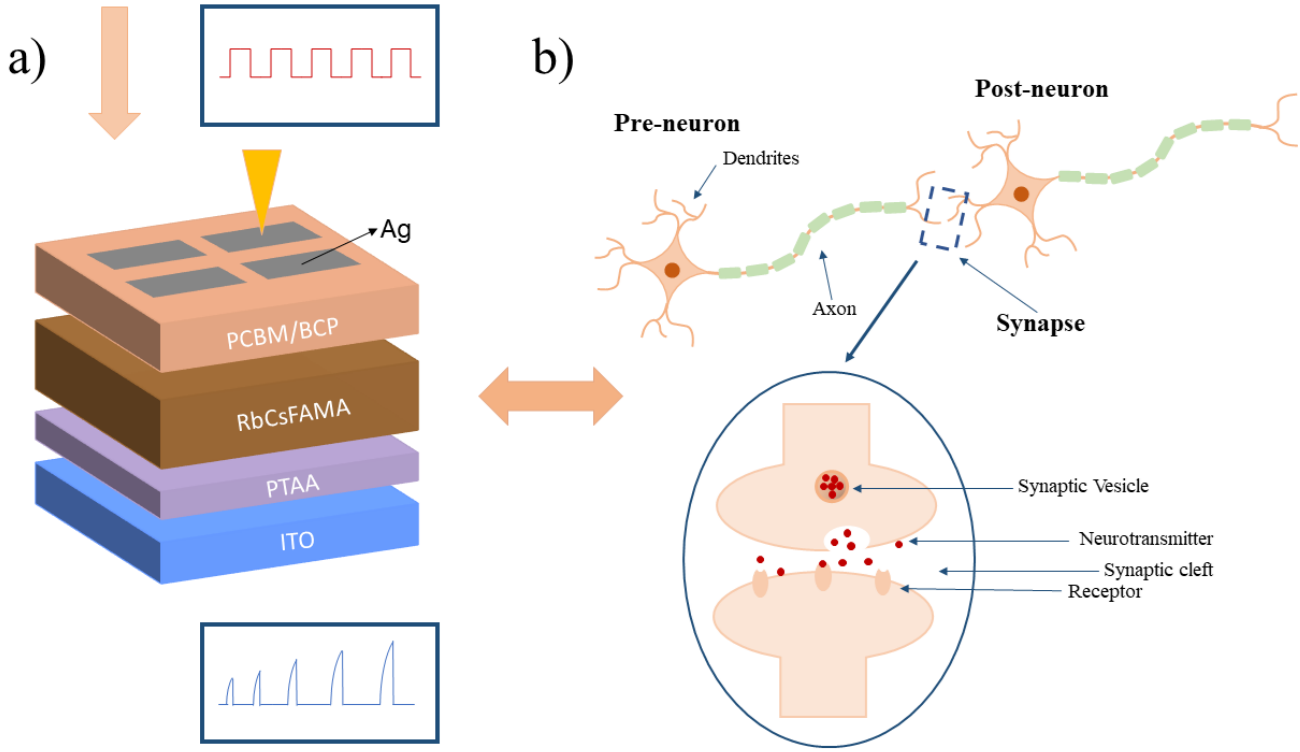

Figure 1 a) Schematic illustration of the perovskite synaptic memory device and b) The biological synapse equivalent.

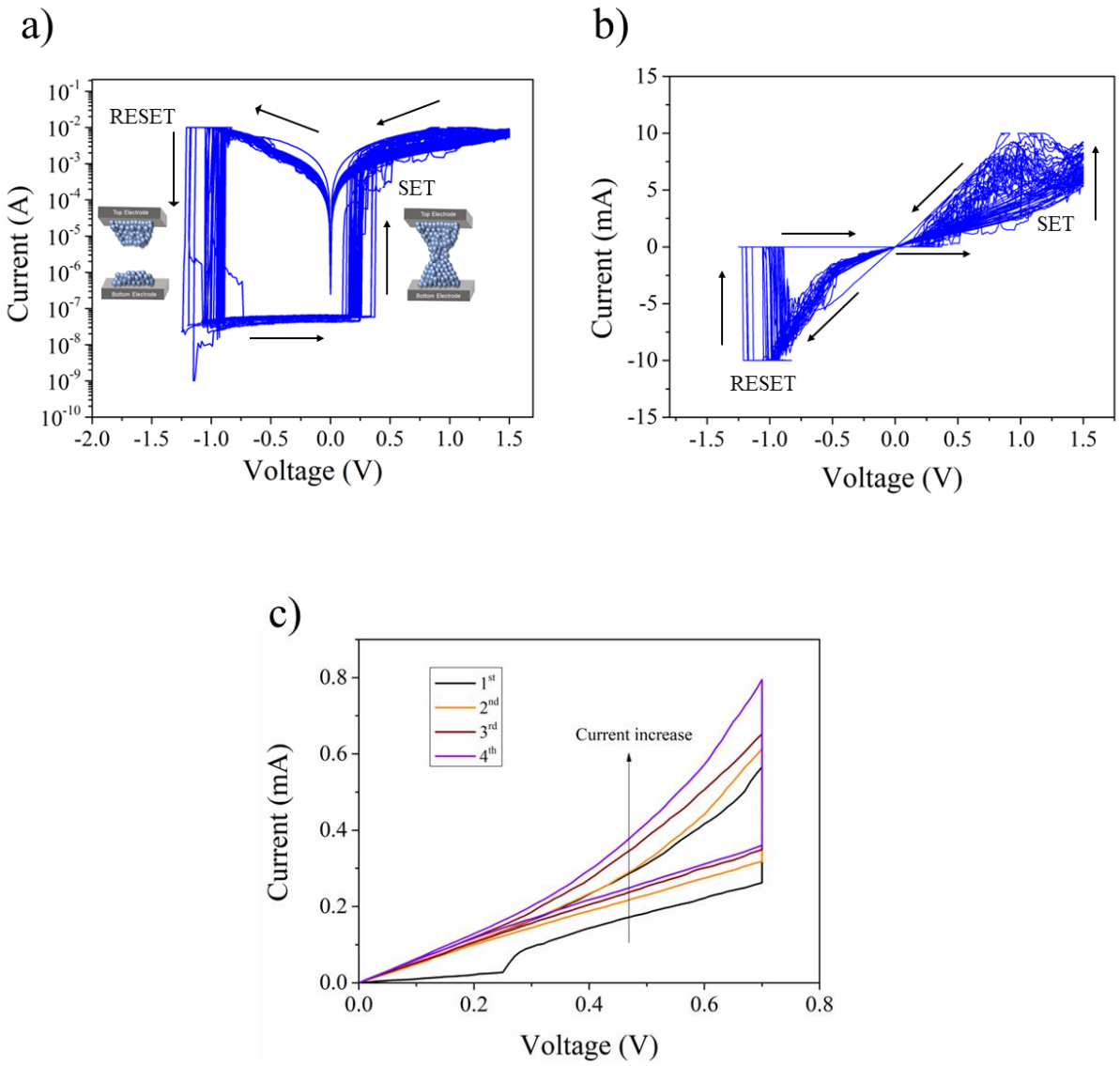

Figure 2 30 I-V Resistive switching loops of the RbCsFAMA synaptic Device in a) Logarithmic and b) Linear Scale, c) Four Consecutive I-V sweeps from 0V to 700mV to 0V.

.

Synaptic plasticity refers to the ability of synaptic weight to change due to neural activity, as neurons can process and transfer information in the form of electrical or chemical signals. Synaptic plasticity is either short-term (STP) or long-term (LTP). The duration of STP lies between tens of milliseconds up to minutes [75]. Paired pulse facilitation (PPF) is a form of short-term plasticity where the amplitude of the second successive post-synaptic potential is enhanced after a pair of stimuli that has sufficient time interval. In biological systems, this enhancement stems from the fact that when the pre-synaptic Ca^{2+} concentration increases, more neurotransmitters are released. In our system, when we apply two consecutive pulses of

500µs duration and 1V amplitude each, the current response produced by the second pulse is larger than the first, leading to the experimental observation of PPF (Figure 3a). The PPF index is defined as:

$$PPF = \frac{A_2 - A_1}{A_1} \times 100\%$$

where A_2 and A_1 are the amplitudes of the first and second pulse. We then investigated the variation of PPF with the delay time between the spikes. Figure 3b presents PPF as a function of the time interval. When the time interval between the pulses increases from 100 to 700 µs, the PPF ratio drops from nearly 45% to almost 2%.

In biological systems, long-term potentiation (LTP) and long-term depression (LTD) are associated with the learning and memory processes [76,77]. Here, we emulate the LTP and LTD process by applying two consecutive pulse trains: the first train consists of 30 pulses of 600mV in amplitude and 3ms duration, and the second train consists of 30 pulses of -300mV in amplitude and 3ms duration. During the first pulses train, the current gradually increases and eventually reaches a saturation region, corresponding to an enhancement of the synaptic weight. The gradual increase in current is due to the modulation of the conductive filament between the Ag top electrode and the ITO bottom electrode. During the second pulses train of negative pulses, the current decreases continuously, leading to a reduced synaptic weight and compensation of the learning process in the memristor [78]. The gap between the LTP and LTD region in our device is due to the rapid rupture of the conductive filament between the two electrodes [79]. The LTP and LTD processes are shown in figure 3c. In addition, we demonstrate that our device can successfully emulate the LTP and LTD process several times with high reproducibility, according to Figure 3d.

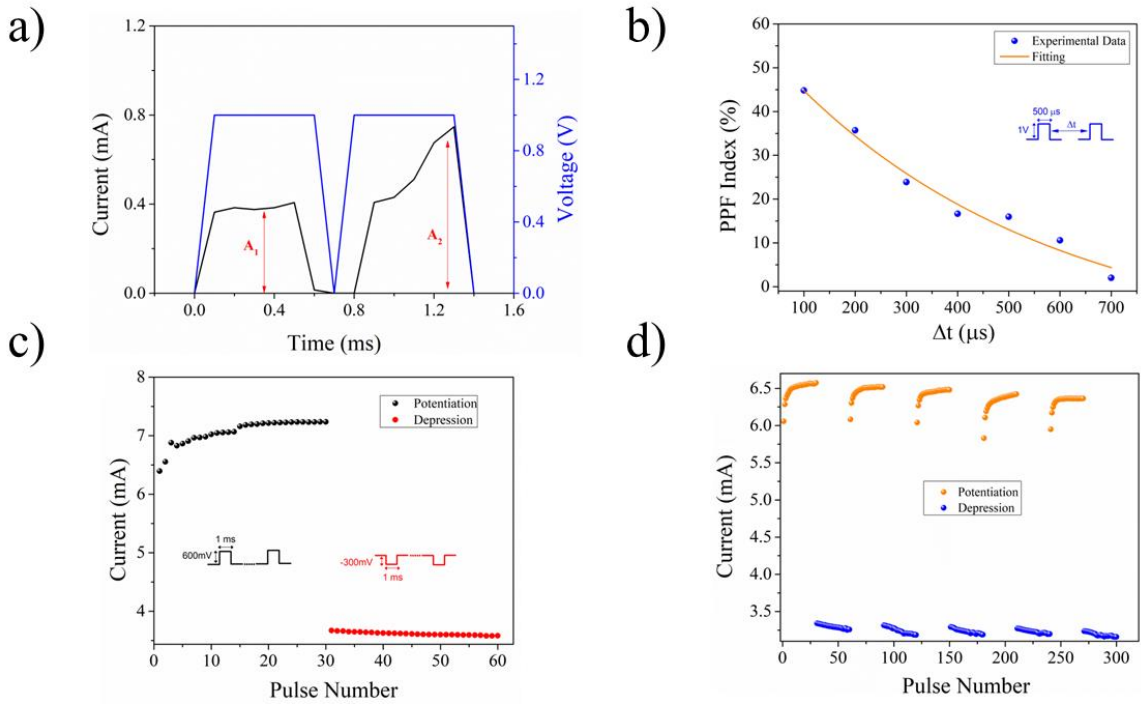

Figure 3 a) Illustration of PPF. b) PPF as a function of Delay time, c) single and d) multiple LTP/LTD cycles.

Our device exhibits another synaptic characteristic, namely the spike-number-dependent plasticity (SNDP). For SNDP implementation, we applied 50 consecutive pulses of 1V amplitude and 200ms

duration. Then, the SNDP ratio defined as I_n/I_1, is obtained and plotted versus the pulses number in Figure 4a. It is evident that as the number of consecutive pulses increases, so does the SNDP ratio. Our synaptic device also possesses a spike-width-dependent plasticity (SWDP), as illustrated in Figure 4b. In this case, we apply pulses of fixed amplitude (600mV) for a variable duration of 0.1, 0.5, 1,5,10,50,100, and 200ms. The current increases with pulse duration, suggesting that increasing the pulse width enhances the synaptic weight. However, for large durations, this increase reaches a saturation point. Spike-Rate-Dependent Plasticity (SRDP) is another synapse feature that depends on the frequency of the spikes. For this measurement, we apply 10 identical spikes of 600mV amplitude and 1ms duration, for a repetition frequency of 10,200 and 500Hz. It is evident from Figure 4c that increasing the frequency results in larger enhancements of the post-synaptic current by comparing the first and the tenth pulse of each frequency set (inset in Figure 4c).

In 1949, Hebbian proposed his theory to explain synaptic plasticity and how neurons adapt during the learning process[80,81]. Spike-timing-dependent plasticity (STDP) is another property of biological synaptic systems and a form of Hebbian learning where synaptic modification depends on the timing and order of pre-and post-synaptic spikes. STDP can be either symmetric or asymmetric[82]. The most common STDP learning rule is asymmetric and is either Hebbian or anti-Hebbian. In all cases, the connection strength between synapses varies exponentially with the delay between the pre-and post-synaptic spikes[83]. Symmetric STDP is also a crucial synaptic function and is more robust than the anti-symmetric one, as it allows information storage and recalls in the hippocampal CA3 network[84]. In our system, we emulate the symmetric anti-Hebbian rule by applying two simple, non-overlapping spikes as square voltage pulses of ±600mV in amplitude and duration of 3ms. The time interval $\Delta t = t_{post} - t_{pre}$ is >0 when the post-synaptic spike is set before the pre-synaptic pulse and negative when the pre-spike is set before the post-spike. When the 600mV post-spike is set before the pre-spike, the synaptic weight potentiates, and when the -600mV pre-spike arrives first, the weight depresses. For synaptic weight calculation, a read pulse of 50mV extracts the current before and after the spikes. The synaptic weight change is the percentage change of the current prior (G_i) and after the spikes (G_f) and is defined as:

$$\Delta W = \frac{G_f - G_i}{G_i} \times 100\%$$

Figure 4d depicts the synaptic weight change as a function of the spike time interval Δt. The data show a STDP-like behavior, while a Gaussian function of the following form was used to fit the data:

$$\Delta W = A \cdot exp\left(\frac{-\Delta t^2}{2\tau^2}\right) + W_0$$

, where A is a scaling factor and τ is the time constant. The fitting process revealed a τ = 459ms, which is on the same order of magnitude as the timescale of synaptic weight modification in biological synapses[85,86], and similar to another report [87].

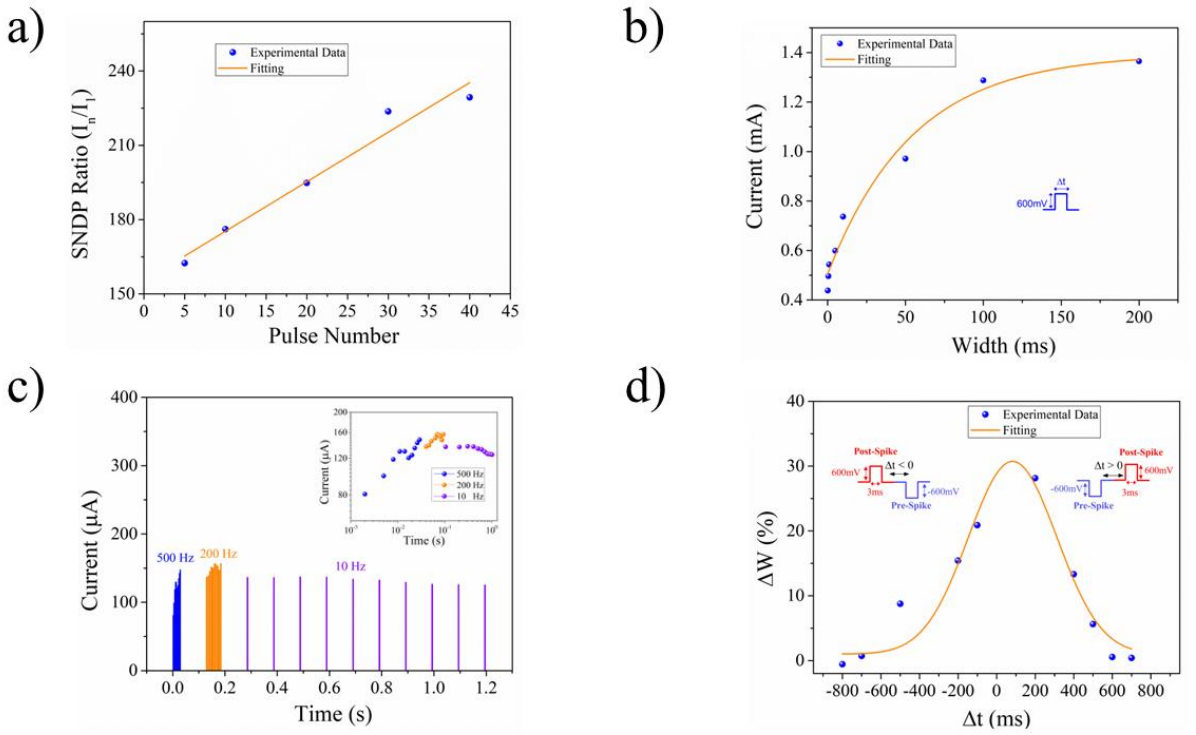

Figure 4 a) Spike-number-dependent plasticity (SNDP) Ratio as a function of pulse number. b) Post-Synaptic Current as a function of pulse width (SWDP). c) SRDP measurement for 10,200 and 500Hz frequency and current enhancement (inset) d) Experimental evidence of STDP.

3 Conclusions

In this work, we extend our previous study on the synaptic properties of a four-cation RbCsFAMA memristive OIHP-based solar cell device. The device operates as an efficient solar cell and concurrently exhibits stable, bipolar resistive switching characteristics with an HRS to LRS ratio of up to 10^5 while operates with low power consumption (operation pulses < ±1V). We show that our device can emulate a series of synaptic functionalities, while the most significant include LTP, LTD, PPF, SRDP, and STDP. Overall, we demonstrate that a mixed cation OIHP system, apart from solar energy harvesting, can also exhibit synaptic and memory behavior.

4 Materials and Methods

Patterned glass/ITO substrates (Naranjo) with a sheet resistance of ~ 20 Ω sq^{-1} were cleaned by subsequent ultrasonication in a liquid soap solution, deionized water, acetone, and isopropanol bath for 10 minutes each. The samples were dried using nitrogen flow, following an oxygen plasma treatment for 5 minutes. Then, a 2mg ml^{-1} solution of Poly[bis(4-phenyl) (2,4,6-trimethylphenyl)amine (PTAA, Solaris) in toluene (Honeywell Research chemicals,≥99.7%) was spin-coated at 6000rpm for 30s. The samples were annealed at 110˚C for 10 minutes. Preparation of quadruple cation-based $Cs_{0.05}Rb_{0.04}(FA_{0.85}MA_{0.15})_{0.91}Pb(I_{0.85}Br_{0.15})_3$

perovskite solution is the same with previous reports[88–90]. 45μl of the solution were dynamically spin-coated on PTAA films at 6000 rpm for 45 s. Then, 200 μl Chlorobenzene (99.8%, anhydrous, Sigma Aldrich) were dropped 20s before the end of the spinning processes, following an annealing at 100˚C for 45 minutes. The $PC_{60}BM$ (99%, Solenne) electron transport layer was deposited by spin coating a 20 mg ml^{-1} solution in Chlorobenzene at 2000 rpm for 60s. Then, a 0.5 mg ml^{-1} bathocuproine solution (BCP) (96%, Sigma Aldrich) in isopropanol (IPA,99.5% extra dry, ACROS Organics,) was spin coated at 4000 rpm for 45 s. Finally, 100 nm Ag were thermally evaporated under a high vacuum of 10^{-6} mbar. For memristive and synaptic measurements, the commercially available platform ARKEO (Cicci Research s.r.l.) was used. Spring probes were attached to the pre- and post- synaptic electrodes. The I-V characteristics of the memristor were captured by sweeping the voltage from -1.5V to 1.5 under 10mA compliance current, with a scan rate of 100mV s^{-1}. For pulse measurements, a custom module by Cicci Research was developed. The module allows the custom design of waveform pulses. During all measurements, the voltage was applied to Ag top electrode while the ITO electrode was grounded. All measurements were performed in ambient air with controlled humidity (30-40%) at 25˚C under dark conditions.

Acknowledgments The work has been supported by the European Union's Horizon 2020 research and innovation program under project EMERGE. The EMERGE project has received funding under grant agreement no. 101008701

Author Contributions M. Loizos fabricated and measured the memristive solar cell devices. K. Rogdakis and E. Kymakis assisted M. Loizos with data analysis and interpretation, while supervised and designed the experiments. M. Loizos wrote the manuscript with inputs from K. Rogdakis and E. Kymakis**.**

Data availability

Declarations

Competing interests. The authors declare no competing interests.

References

1. Ahmed E, Yaqoob I, Hashem IAT, Khan I, Ahmed AIA, Imran M, et al. The role of big data analytics in Internet of Things. Computer Networks. 2017;129:459–471.

2. Backus J. Can programming be liberated from the von Neumann style? a functional style and its algebra of programs. Comput. Netw. 1978;21:613–641.

3. Merolla PA, Arthur JV, Alvarez-Icaza R, Cassidy AS, Sawada J, Akopyan F, et al. A million spiking-neuron integrated circuit with a scalable communication network and interface. Science. 2014;345:668–673.

4. Ho VM, Lee J-A, Martin KC. The Cell Biology of Synaptic Plasticity. Science. 2011;334:623–628.

5. Sarkar D, Tao J, Wang W, Lin Q, Yeung M, Ren C, et al. Mimicking Biological Synaptic Functionality with an Indium Phosphide Synaptic Device on Silicon for Scalable Neuromorphic Computing. ACS Nano. 2018;12:1656–1663.

6. Citri A, Malenka RC. Synaptic Plasticity: Multiple Forms, Functions, and Mechanisms. Neuropsychopharmacol. 2008;33:18–41.

7. Abbott LF, Nelson SB. Synaptic plasticity: taming the beast. Nat. Neurosci. 2000;3:1178–1183.

8. Laughlin SB, de Ruyter van Steveninck RR, Anderson JC. The metabolic cost of neural information. Nat. Neurosci. 1998;1:36–41.

9. Xiong W, Liu L, Liu J, Chen W, Zheng Y. Phase field study on the performance of artificial synapse device based on the motion of domain wall in ferroelectric thin films. Appl. Phys. Lett. 2021;118:242902.

10. Jo SH, Chang T, Ebong I, Bhadviya BB, Mazumder P, Lu W. Nanoscale Memristor Device as Synapse in Neuromorphic Systems. Nano Lett. 2010;10:1297–1301.

11. Choi S, Jang S, Moon J-H, Kim JC, Jeong HY, Jang P, et al. A self-rectifying TaO_y/nanoporous TaO_x memristor synaptic array for learning and energy-efficient neuromorphic systems. NPG Asia Mater. 2018;10:1097–1106.

12. Abbas H, Abbas Y, Hassan G, Sokolov AS, Jeon Y-R, Ku B, et al. The coexistence of threshold and memory switching characteristics of ALD HfO_2 memristor synaptic arrays for energy-efficient neuromorphic computing. Nanoscale. 2020;12:14120–14134.

13. Shen AM, Chen C-L, Kim K, Cho B, Tudor A, Chen Y. Analog Neuromorphic Module Based on Carbon Nanotube Synapses. ACS Nano. 2013;7:6117–6122.

14. Wan CJ, Zhu LQ, Liu YH, Feng P, Liu ZP, Cao HL, et al. Proton-Conducting Graphene Oxide-Coupled Neuron Transistors for Brain-Inspired Cognitive Systems. Adv. Mater. 2016;28:3557–3563.

15. Kim Y, Chortos A, Xu W, Liu Y, Oh JY, Son D, et al. A bioinspired flexible organic artificial afferent nerve. Science. 2018;360:998–1003.

16. Kuzum D, Jeyasingh RGD, Lee B, Wong H-SP. Nanoelectronic Programmable Synapses Based on Phase Change Materials for Brain-Inspired Computing. Nano Lett. 2012;12:2179–2186.

17. Suri M, Bichler O, Querlioz D, Cueto O, Perniola L, Sousa V, et al. Phase change memory as synapse for ultra-dense neuromorphic systems: Application to complex visual pattern extraction. 2011 IEDM. 2011. p. 4.4.1-4.4.4.

18. Chen L, Wang T-Y, Dai Y-W, Cha M-Y, Zhu H, Sun Q-Q, et al. Ultra-low power $Hf_{0.5}Zr_{0.5}O_2$ based ferroelectric tunnel junction synapses for hardware neural network applications. Nanoscale. 2018;10:15826–15833.

19. Yoon C, Lee JH, Lee S, Jeon JH, Jang JT, Kim DH, et al. Synaptic Plasticity Selectively Activated by Polarization-Dependent Energy-Efficient Ion Migration in an Ultrathin Ferroelectric Tunnel Junction. Nano Lett. 2017;17:1949–1955.

20. Liu T, Yan TH, Scheuerlein R, Chen Y, Lee JK, Balakrishnan G, et al. A 130.7-$\hboxmm^2$ 2-Layer 32-Gb ReRAM Memory Device in 24-nm Technology. IEEE Journal of Solid-State Circuits. 2014;49:140–53.

21. Golonzka O, Arslan U, Bai P, Bohr M, Baykan O, Chang Y, et al. Non-Volatile RRAM Embedded into 22FFL FinFET Technology. 2019 Symposium on VLSI Technology. 2019. p. T230–231.

22. Chiu Y-C, Hu H-W, Lai L-Y, Huang T-Y, Kao H-Y, Chang K-T, et al. A 40nm 2Mb ReRAM Macro with 85% Reduction in FORMING Time and 99% Reduction in Page-Write Time Using Auto-FORMING and Auto-Write Schemes. 2019 Symposium on VLSI Technology. 2019. p. T232–233.

23. Yan X, Zhao J, Liu S, Zhou Z, Liu Q, Chen J, et al. Memristor with Ag-Cluster-Doped TiO_2 Films as Artificial Synapse for Neuroinspired Computing. Adv. Funct. Mater. 2018;28:1705320.

24. Kim S, Du C, Sheridan P, Ma W, Choi S, Lu WD. Experimental Demonstration of a Second-Order Memristor and Its Ability to Biorealistically Implement Synaptic Plasticity. Nano Lett. 2015;15:2203–2211.

25. Yao P, Wu H, Gao B, Tang J, Zhang Q, Zhang W, et al. Fully hardware-implemented memristor convolutional neural network. Nature. 2020;577:641–646.

26. Wang Z, Joshi S, Savel'ev S, Song W, Midya R, Li Y, et al. Fully memristive neural networks for pattern classification with unsupervised learning. Nat. Electron. 2018;1:137–145.

27. Zidan MA, Strachan JP, Lu WD. The future of electronics based on memristive systems. Nat. Electron. 2018;1:22–29.

28. Xu R, Jang H, Lee M-H, Amanov D, Cho Y, Kim H, et al. Vertical MoS_2 Double-Layer Memristor with Electrochemical Metallization as an Atomic-Scale Synapse with Switching Thresholds Approaching 100 mV. Nano Lett. 2019;19:2411–2417.

29. Shi Y, Liang X, Yuan B, Chen V, Li H, Hui F, et al. Electronic synapses made of layered two-dimensional materials. Nat. Electron. 2018;1:458–465.

30. Yan X, Zhao Q, Chen AP, Zhao J, Zhou Z, Wang J, et al. Vacancy-Induced Synaptic Behavior in 2D WS_2 Nanosheet–Based Memristor for Low-Power Neuromorphic Computing. Small. 2019;15:1901423.

31. Li S, Zeng F, Chen C, Liu H, Tang G, Gao S, et al. Synaptic plasticity and learning behaviours mimicked through Ag interface movement in an Ag/conducting polymer/Ta memristive system. J Mater. Chem. C. 2013;1:5292–5298.

32. Jang BC, Kim S, Yang SY, Park J, Cha J-H, Oh J, et al. Polymer Analog Memristive Synapse with Atomic-Scale Conductive Filament for Flexible Neuromorphic Computing System. Nano Lett. 2019;19:839–849.

33. Raifuku I, Chao Y-P, Chen H-H, Lin C-F, Lin P-E, Shih L-C, et al. Halide perovskite for low-power consumption neuromorphic devices. EcoMat. 2021;3:e12142.

34. Xu W, Cho H, Kim YH, Kim YT, Wolf C, Park CG, et al. Organometal Halide Perovskite Artificial Synapses. Adv. Mater. 2016;28:5916–5922.

35. Wang T-Y, Meng J-L, Li Q-X, He Z-Y, Zhu H, Ji L, et al. Reconfigurable optoelectronic memristor for in-sensor computing applications. Nano Energy. 2021;89:106291.

36. Zhong Y, Tang J, Li X, Gao B, Qian H, Wu H. Dynamic memristor-based reservoir computing for high-efficiency temporal signal processing. Nat. Commun. 2021;12:408.

37. Gong J, Wei H, Ni Y, Zhang S, Du Y, Xu W. Methylammonium halide-doped perovskite artificial synapse for light-assisted environmental perception and learning. Mater. Today Phys. 2021;21:100540.

38. Wang K, Li L, Zhao R, Zhao J, Zhou Z, Wang J, et al. A Pure 2H-MoS_2 Nanosheet-Based Memristor with Low Power Consumption and Linear Multilevel Storage for Artificial Synapse Emulator. Adv. Electron. Mater. 2020;6:1901342.

39. Lee S-H, Park H-L, Kim M-H, Kim M-H, Park B-G, Lee S-D. Realization of Biomimetic Synaptic Functions in a One-Cell Organic Resistive Switching Device Using the Diffusive Parameter of Conductive Filaments. ACS Appl. Mater. Interfaces. 2020;12:51719–51728.

40. Lanza M, Sebastian A, Lu WD, Le Gallo M, Chang M-F, Akinwande D, et al. Memristive technologies for data storage, computation, encryption, and radio-frequency communication. Science. 2022;376:eabj9979.

41. Mohammad B, Jaoude MA, Kumar V, Al Homouz DM, Nahla HA, Al-Qutayri M, et al. State of the art of metal oxide memristor devices. Nanotechnol. Rev. 2016;5:311–329.

42. Dong Q, Fang Y, Shao Y, Mulligan P, Qiu J, Cao L, et al. Electron-hole diffusion lengths > 175 μm in solution-grown $CH_3NH_3PbI_3$ single crystals. Science. 2015;347:967–970.

43. Li F, Ma C, Wang H, Hu W, Yu W, Sheikh AD, et al. Ambipolar solution-processed hybrid perovskite phototransistors. Nat. Commun. 2015;6:8238.

44. Herz LM. Charge-Carrier Mobilities in Metal Halide Perovskites: Fundamental Mechanisms and Limits. ACS Energy Lett. 2017;2:1539–1548.

45. Eperon GE, Stranks SD, Menelaou C, Johnston MB, Herz LM, Snaith HJ. Formamidinium lead trihalide: a broadly tunable perovskite for efficient planar heterojunction solar cells. Energy Environ. Sci. 2014;7:982–988.

46. Jena AK, Kulkarni A, Miyasaka T. Halide Perovskite Photovoltaics: Background, Status, and Future Prospects. Chem. Rev. 2019;119:3036–3103.

47. Kim JY, Lee JW, Jung HS, Shin H, Park NG. High-Efficiency Perovskite Solar Cells. Chem. Rev. 2020;120: 7867-7918.

48. Jiang J, Chu Z, Yin Z, Li J, Yang Y, Chen J, et al. Red Perovskite Light-Emitting Diodes with Efficiency Exceeding 25% Realized by Co-Spacer Cations. Adv. Mater. 2022;34:2204460.

49. Gagaoudakis E, Panagiotopoulos A, Maksudov T, Moschogiannaki M, Katerinopoulou D, Kakavelakis G, et al. Self-powered, flexible and room temperature operated solution processed hybrid metal halide p-type sensing element for efficient hydrogen detection. J Phys. Mater. 2020;3:014010.

50. Park H-L, Lee T-W. Organic and perovskite memristors for neuromorphic computing. Org. Electron. 2021;98:106301.

51. Miao J, Zhang F. Recent progress on highly sensitive perovskite photodetectors. J Mater. Chem. C. 2019;7:1741–1791.

52. Liu Y, Chen P-A, Hu Y. Recent developments in fabrication and performance of metal halide perovskite field-effect transistors. J Mater. Chem. C. 2020;8:16691–16715.

53. Yoo JJ, Seo G, Chua MR, Park TG, Lu Y, Rotermund F, et al. Efficient perovskite solar cells via improved carrier management. Nature. 2021;590:587-593.

54. Zhao Y, Ma F, Qu Z, Yu S, Shen T, Deng H-X, et al. Inactive $(PbI_2)_2RbCl$ stabilizes perovskite films for efficient solar cells. Science. 2022;377:531–534.

55. Younis A, Lin C-H, Guan X, Shahrokhi S, Huang C-Y, Wang Y, et al. Halide Perovskites: A New Era of Solution-Processed Electronics. Adv. Mater. 2021;33:2005000.

56. Kang DH, Park NG. On the Current–Voltage Hysteresis in Perovskite Solar Cells: Dependence on Perovskite Composition and Methods to Remove Hysteresis. Adv. Mater. 2019;31: 1805214

57. Yang JJ, Strukov DB, Stewart DR. Memristive devices for computing. Nat. Nanotechnol. 2013;8:13–24.

58. Jeong DS, Thomas R, Katiyar RS, Scott JF, Kohlstedt H, Petraru A, et al. Emerging memories: resistive switching mechanisms and current status. Rep. Prog. Phys. 2012;75:076502.

59. Xiao X, Hu J, Tang S, Yan K, Gao B, Chen H, et al. Recent Advances in Halide Perovskite Memristors: Materials, Structures, Mechanisms, and Applications. Adv. Mater. Technol. 2020;5: 1900914.

60. Eames C, Frost JM, Barnes PRF, O'Regan BC, Walsh A, Islam MS. Ionic transport in hybrid lead iodide perovskite solar cells. Nat. Commun. 2015;6:7497.

61. Xiao Z, Huang J. Energy-Efficient Hybrid Perovskite Memristors and Synaptic Devices. Adv. Electron. Mater. 2016;2:1600100.

62. Lao J, Xu W, Jiang C, Zhong N, Tian B, Lin H, et al. Artificial Synapse Based on Organic–Inorganic Hybrid Perovskite with Electric and Optical Modulation. Adv. Electron. Mater. 2021;7:2100291.

63. Ma F, Zhu Y, Xu Z, Liu Y, Zheng X, Ju S, et al. Optoelectronic Perovskite Synapses for Neuromorphic Computing. Adv. Funct. Mater. 2020;30:1908901.

64. Tian H, Zhao L, Wang X, Yeh YW, Yao N, Rand BP, et al. Extremely Low Operating Current Resistive Memory Based on Exfoliated 2D Perovskite Single Crystals for Neuromorphic Computing. ACS Nano. 2017;11:12247–12256.

65. Kim SI, Lee Y, Park MH, Go GT, Kim YH, Xu W, et al. Dimensionality Dependent Plasticity in Halide Perovskite Artificial Synapses for Neuromorphic Computing. Adv. Electron. Mater. 2019;5:1900008.

66. John RA, Demirağ Y, Shynkarenko Y, Berezovska Y, Ohannessian N, Payvand M, et al. Reconfigurable halide perovskite nanocrystal memristors for neuromorphic computing. Nat. Commun. 2022;13:2074.

67. Ye H, Liu Z, Han H, Shi T, Liao G. Lead-free $AgBiI_4$ perovskite artificial synapses for a tactile sensory neuron system with information preprocessing function. Mater. Adv. 2022;3:7248-7256

68. John RA, Yantara N, Ng YF, Narasimman G, Mosconi E, Meggiolaro D, et al. Ionotronic Halide Perovskite Drift-Diffusive Synapses for Low-Power Neuromorphic Computation. Adv. Mater. 2018;30:1805454.

69. Yu H, Wei H, Gong J, Han H, Ma M, Wang Y, et al. Evolution of Bio-Inspired Artificial Synapses: Materials, Structures, and Mechanisms. Small. 2021;17:2000041.

70. Zhang S-R, Zhou L, Mao J-Y, Ren Y, Yang J-Q, Yang G-H, et al. Artificial Synapse Emulated by Charge Trapping-Based Resistive Switching Device. Adv. Mater. Technol. 2019;4:1800342.

71. Lao J, Xu W, Jiang C, Zhong N, Tian B, Lin H, et al. An air-stable artificial synapse based on a lead-free double perovskite $Cs_2AgBiBr_6$ film for neuromorphic computing. J Mater. Chem. C. 2021;9:5706–5712.

72. Rogdakis K, Loizos M, Viskadouros G, Kymakis E. Memristive perovskite solar cells towards parallel solar energy harvesting and processing-in-memory computing. Mater. Adv. 2022;3:7002-7014

73. Zhu X, Lee J, Lu WD. Iodine Vacancy Redistribution in Organic–Inorganic Halide Perovskite Films and Resistive Switching Effects. Adv. Mater. 2017;29:1700527.

74. Lee S, Choi J, Jeon JB, Kim BJ, Han JS, Kim TL, et al. Conducting Bridge Resistive Switching Behaviors in Cubic $MAPbI_3$, Orthorhombic $RbPbI_3$, and Their Mixtures. Adv. Electron. Mater. 2019;5:1800586.

75. Zucker RS, Regehr WG. Short-Term Synaptic Plasticity. Annu. Rev. Physiol. 2002;64:355–405.

76. Whitlock JR, Heynen AJ, Shuler MG, Bear MF. Learning induces long-term potentiation in the hippocampus. Science. 2006;313:1093–1097.

77. Whalley K. Balancing LTP and LTD. Nat. Rev. Neurosci. 2007;8: 249.

78. Choi H-W, Song K-W, Kim S-H, Nguyen KT, Eadi SB, Kwon H-M, et al. Zinc oxide and indium-gallium-zinc-oxide bi-layer synaptic device with highly linear long-term potentiation and depression characteristics. Sci. Rep. 2022;12:1259.

79. Gil Kim S, Van Le Q, Su Han J, Kim H, Choi M-J, Lee SA, et al. Dual-Phase All-Inorganic Cesium Halide Perovskites for Conducting-Bridge Memory-Based Artificial Synapses. Adv. Funct. Mater. 2019;29:1906686.

80. Caporale N, Dan Y. Spike Timing–Dependent Plasticity: A Hebbian Learning Rule. Annu. Rev. Neurosci. 2008;31:25–46.

81. Brown RE, Milner PM. The legacy of Donald O. Hebb: more than the Hebb Synapse. Nat. Rev. Neurosci. 2003;4:1013–1019.

82. Koch G, Ponzo V, Lorenzo FD, Caltagirone C, Veniero D. Hebbian and Anti-Hebbian Spike-Timing-Dependent Plasticity of Human Cortico-Cortical Connections. J Neurosci. 2013;33:9725–9733.

83. Zhu J, Zhang T, Yang Y, Huang R. A comprehensive review on emerging artificial neuromorphic devices. Appl. Phys. Rev. 2020;7:011312.

84. Mishra R, Kim S, Guzman S et al. Symmetric spike timing-dependent plasticity at CA3–CA3 synapses optimizes storage and recall in autoassociative networks Nat. Commun. 2016;7:11552.

85. Kuzum D, Yu S, Wong H-SP. Synaptic electronics: materials, devices and applications. Nanotechnology. 2013;24:382001.

86. Markram H, Lübke J, Frotscher M, Sakmann B. Regulation of synaptic efficacy by coincidence of postsynaptic APs and EPSPs. Science. 1997;275:213–215.

87. Zhang C, Ye WB, Zhou K, Chen H-Y, Yang J-Q, Ding G, et al. Bioinspired Artificial Sensory Nerve Based on Nafion Memristor. Adv. Funct. Mater. 2019;29:1808783.

88. Chatzimanolis K, Rogdakis K, Tsikritzis D, Tzoganakis N, Tountas M, Krassas M, et al. Inverted perovskite solar cells with enhanced lifetime and thermal stability enabled by a metallic tantalum disulfide buffer layer. Nanoscale Adv. 2021;3:3124–3135.

89. Tzoganakis N, Feng B, Loizos M, Krassas M, Tsikritzis D, Zhuang X, et al. Ultrathin PTAA interlayer in conjunction with azulene derivatives for the fabrication of inverted perovskite solar cells. J Mater. Chem. C. 2021;9:14709–14719.

90. Loizos M, Tountas M, Tzoganakis N, Chochos CL, Nega A, Schiza A, et al. Enhancing the lifetime of inverted perovskite solar cells using a new hydrophobic hole transport material. Energy Adv. 2022;1:312–320.